Available online at www.sciencedirect.com
ScienceDirect
Journal of Power Sources 165 (2007) 368–378
JOURNAL OF POWER SOURCES
www.elsevier.com/locate/jpowsour

Silicon, graphite and resin based hard carbon nanocomposite anodes for lithium ion batteries

Moni Kanchan Datta [a], Prashant N. Kumta [a,b,*]

[a] *Department of Materials Science and Engineering, Carnegie Mellon University, Pittsburgh, PA 15213, USA*
[b] *Department of Biomedical Engineering, Carnegie Mellon University, Pittsburgh, PA 15213, USA*

Received 20 November 2006; received in revised form 8 December 2006; accepted 11 December 2006
Available online 16 December 2006

Abstract

Nanocomposite based on graphite (C), silicon (Si) and poly[(*o*-cresyl glycidyl ether)-*co*-formaldehyde] resin based amorphous hard carbon (HC), denoted as Si/C/HC, have been synthesized by thermal treatment of mechanically milled graphite, silicon and resin of nominal composition C–18 wt.% Si–40 wt.% resin at 973 K, 1073 K and 1173 K in ultrahigh purity argon atmosphere. The formation of the electrochemically inactive SiC is bypassed as well as the amorphization kinetics of graphite is reduced during prolonged milling of graphite and Si in the presence of the resin. Microstructural analysis has confirmed that the Si nanoparticle gets embedded, and is homogeneously dispersed and distributed on the graphite matrix after mechanical milling as well as after thermal treatment. Electrochemical studies have revealed that the Si/C/HC based nanocomposite, tested as a lithium ion anode, synthesized after thermal treatment at 1173 K exhibits a stable capacity of ∼640 mAh g^{-1} with an excellent capacity retention when cycled at a rate of ∼160 mA g^{-1}. The nanocomposite anode also shows a moderate rate capability when cycled at different discharge/charge rates. Scanning electron microscopy analysis indicates that the structural integrity and the microstructural stability of the nanocomposite during the alloying/dealloying process contribute to the good cyclability observed in the above nanocomposites.

Keywords: Mechanical alloying; Si/C/HC nanocomposite; Anode; Li ion battery

1. Introduction

Rechargeable lithium ion batteries exhibiting high energy and high power density are in great demand as energy sources for a variety of advanced technologies. Commercial lithium ion batteries at present employ the use of graphitic carbon anode which provides a theoretical capacity of 372 mAh g^{-1} [1–3]. However, the demand for new compact and modern portable electronic devices as well as for hybrid electric vehicles, portable power tools and backup power makes it even more critical for the availability of higher energy density power sources with excellent cyclability and high rate capability. Lithium storage anodes based on the alloying of lithium with metals and metalloids such as Sn, Si, Al and Sb are considered to be attractive alternatives to graphite due to their low cost and high energy densities, which are up to an order of magnitude higher than that of graphitized carbon [2–4]. However, the severe crystallographic volume changes that occur during the alloying and dealloying processes of lithium lead to mechanical failure of the anode resulting in decrepitation and crumbling of the electrodes [2–5]. This effect seriously compromises the cycling efficiency, cycle life and rate capability of Li ion cells due to the loss of electronic particle to particle contact and consequent increase in electrical resistivity of the electrode.

Considerable research efforts have thus been dedicated to overcome this limitation of intermetallic electrodes by using composite materials, in which an electrochemically active phase is homogeneously dispersed within an electrochemically inactive matrix [3,6–10]. The electrochemically inactive phase is preferred to comprise a sufficient volume fraction (∼60–70%) of a soft and ductile matrix, which can accommodate the large mechanical stresses/strains generated and experienced by the active phase. As a result, the structural integrity of the composite electrode can be retained during the alloying and dealloying

* Corresponding author at: Department of Materials Science and Engineering, Carnegie Mellon University, Pittsburgh, PA 15213, USA. Tel.: +1 412 268 8739; fax: +1 412 268 7596.
E-mail address: kumta@cmu.edu (P.N. Kumta).

0378-7753/$ – see front matter © 2007 Elsevier B.V. All rights reserved.
doi:10.1016/j.jpowsour.2006.12.013

processes. In addition, the inactive matrix as well as the active phase must possess high electronic conductivity and high lithium ion diffusivity, respectively, in order to achieve high rate capability.

In recent years, several authors have reported [10–17] that the Si/C based composites, prepared by decomposition of organic precursors and/or using high energy mechanical milling, show higher reversible capacity with respect to graphite and better capacity retention with respect to pure silicon. However, the cycle life of these composite have unfortunately, not met the practical battery requirements due to the deterioration of the composite during cycling. It has been reported [11] that silicon and graphite based composite synthesized by thermal pyrolysis of polyvinyl chloride dispersed with nanosized silicon and fine graphite particles shows a reversible capacity ~700 mAh g^{-1} with better cyclability than nanocrystalline Si alone. Kim and Kumta [12] have reported that Si/C nanocomposite, synthesized by pyrolyzing mechanically milled silicon and polystyrene resin, shows a reversible capacity of ~850 mAh g^{-1} with a reasonable capacity retention (1.1% loss per cycle). On the other hand, Si/C composite, synthesized by moderate ball milling of carbon (graphite, MCMB, disordered carbon, etc.) and nanocrystalline Si [15–17] shows a high first discharge and charge capacity (~800–1400 mAh g^{-1} depending on the compositions studied) but exhibits poor capacity retention, which is not suitable for practical commercial applications. Gross et al. [16] have reported that the Si/C composite, synthesized by mechanical mixing of graphite and premilled Si powder for a period of about 15 min by using SPEX 8000 shaker mill, shows a first charge capacity ~800 mAh g^{-1} with a fade in capacity ~1.25% (~600 mAh g^{-1} after 20 cycles) of nominal composition C–20 wt.% Si. The poor capacity retention of Si/C composite may arise not only due to Si being not homogeneously dispersed and distributed in the carbon matrix, but also due to poor interface adhesion between carbon and Si during the short duration of milling. In this regard, extended milling could be useful to disperse and distribute the active Si phase homogeneously in the graphite matrix. However, the formation of the undesired SiC and amorphization of graphite during prolonged milling (e.g. within ~5 h of milling in SPEX 8000 shaker mill) of graphite and Si [10,18–21] limits the feasibility of mechanical milling to synthesize Si/C composites for possible application as an anode in the Li ion battery industry. In order to achieve the high capacity in excess of graphite with good cyclability in the Si/C based composite, it is of paramount importance to circumvent the formation of SiC during extended milling of graphite and silicon, and form a strong interface bonding between the graphite and Si.

We have recently identified that the addition of polyacrylonitrile (PAN) with graphite and silicon act as a diffusion barrier to the reaction between graphite and silicon to form SiC during extended mechanical milling [10]. The composite comprising silicon and graphite, coated with PAN based disordered carbon, synthesized by thermal treatment of mechanically milled silicon, graphite and PAN, exhibit a reversible capacity of ~660 mAh g^{-1} with an excellent capacity retention [10]. The present study addresses the feasibility of using *o*-cresol novolac epoxy resin with graphite and silicon to bypass the formation of SiC during prolonged milling (~15 h) using the SPEX 8000 shaker mill, and to form a nanocomposite based on silicon, graphite and resin based amorphous hard carbon by thermal treatment of the mechanically milled powder where the active Si nanoparticle is homogeneously dispersed and distributed in the graphite matrix combined with an enhanced interface adhesion between the silicon and graphite by coating with amorphous hard carbon. In addition, a more detailed study on the microstructural evolution during mechanical alloying as well as after thermal treatment and on the rate capability of the thermally treated nanocomposite electrode has been presented in the present article.

2. Experimental details

2.1. Materials synthesis

Mixtures of elemental powders of synthetic graphite (Aldrich, 1–2 μm), Si (Alfa aesar, −325 mesh) and poly[(*o*-cresyl glycidyl ether)-*co*-formaldehyde] based epoxy resin (average $M_n \sim 1080$, Aldrich) of elemental composition C–18 wt.% Si–40 wt.% resin were subjected to mechanical milling in a high energy shaker mill (SPEX CertiPrep 8000M) up to 15 h in a stainless steel (SS) vial using 30 SS balls of 2 mm diameter (~30 g) with a ball to powder weight ratio 10:1. Specifically, 1.2 g of resin was dissolved in ~10 ml *N*-methylpyrrolidinone (NMP) to form a homogeneous solution. Graphite (~1.26 g), Si (~0.54 g) and the resin solution were batched in a vial inside an argon filled glove box (Vacuum Atmosphere HE-493, ~10 ppm oxygen and ~0.10 ppm moisture) in order to prevent oxidation of the reactive components during milling. The resin solution keeps the ingredients and grinding balls completely submerged. This was helpful to avoid excessive cold welding, agglomeration and temperature build up during milling. In order to decompose the resin to form resin based amorphous hard carbon (HC) [22–25], the mechanically milled powders were annealed isothermally at 773 K, 973 K, 1073 K and 1173 K for 6 h at each temperature in an ultrahigh purity argon (UHP-Ar) atmosphere using a heating rate 10 K min^{-1} and a flow rate of 100 mL min^{-1}.

2.2. Materials characterization

In order to perform qualitative phase analysis, the milled powders as well as heat treated powders were characterized by X-ray diffraction (XRD) using the Philips XPERT PRO system employing the Cu Kα ($\lambda = 0.15406$ nm) radiation. Additionally, to identify the decomposition temperature and yield of the resin, differential thermal analysis (DTA) and thermogravimetric analysis (TGA) has been performed on the pure resin. The DTA/TGA experiments were performed in a simultaneous TGA/DTA machine (TA 2960, TA Instrument, New Castle, DE) under UHP-Ar at a heating rate of 10 K min^{-1} using ~17 mg resin. To investigate the microstructure of the as prepared composites as well as the electrochemically cycled sample, scanning electron microscopy (SEM) and transmission

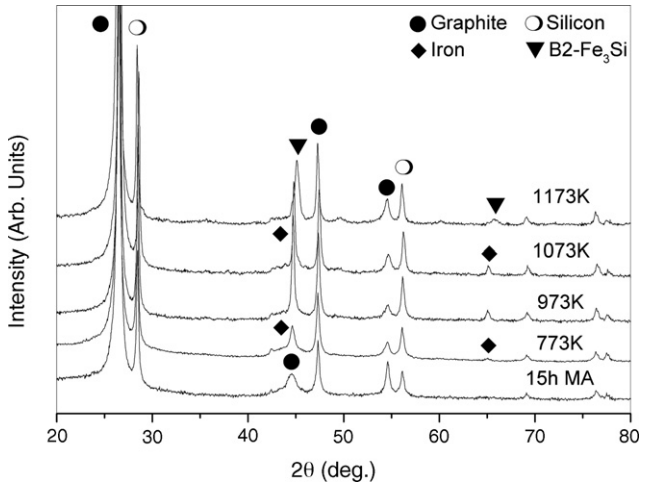

Fig. 1. XRD patterns of C–18 wt.% Si–40 wt.% resin generated after 15 h of milling and after thermal treatment at 773 K, 973 K, 1073 K and 1173 K for 6 h each in UHP argon following the 15 h of milling.

electron microscopy (TEM) analysis was conducted. Quantitative elemental analysis and distribution of the elements (by X-ray mapping) in the composite was further investigated using the energy dispersive X-ray (EDS) analyzer attached with the SEM. Philips XL-30FEG equipped with an EDS detector system comprised of an ultrathin beryllium window and Si(Li) detector operating at 25 kV was employed for the secondary electron (SE) image, elemental and X-ray mapping analyses. JEOL 4000EX operating at 400 kV was employed for conducting TEM analysis to evaluate the particle size and the distribution of phases within the composite. The specific surface area of the composite after mechanical milling as well as after thermal treatment was measured using the BET method from the nitrogen adsorption/desorption data obtained at 77 K using a NOVA2000 (Quantachrome) automatic BET surface area and porosimetry analyses unit. Before measuring the surface area, all the samples (∼0.05 g) were degassed at 423 K for 12 h.

Electrochemical characteristics were analyzed from electrodes that were prepared by mixing 82 wt.% of the active powder of −325 mesh and 8 wt.% acetylene black. A solution containing 10 wt.% polyvinylidene fluoride (PVDF) in *N*-methylpyrrolidinone was added to the mixture. The as-prepared solution was coated onto a Cu foil. A 2016 coin cell design was used employing lithium foil as an anode and 1 M $LiPF_6$ in ethylene carbonate/diethyl carbonate (EC/DEC = 1:2 in volume) as the electrolyte. All the cells tested in this study were cycled at room temperature (∼298 K) in the voltage range from 0.02 to 1.2 V employing different discharge/charge rates (40–160 mA g^{-1}) and a minute rest period between the charge/discharge cycles using a potentiostat (Arbin electrochemical instrument).

3. Results and discussion

Fig. 1 shows the XRD patterns obtained from the graphite–18 wt.% Si–40 wt.% resin composite precursor after 15 h of milling. As shown in Fig. 1, the XRD patterns of the 15 h milled sample show the presence of graphite and silicon without any detectable amount of SiC. The formation of electrochemically inactive SiC, which could be easily formed during high energy mechanical milling (e.g. within ∼5 h of mechanical milling in SPEX 8000 shaker mill) of pure graphite and Si [10,18,19], is bypassed in the presence of the resin solution. In addition, graphite also retains its graphitic structure in the presence of the resin solution even after ∼15 h of milling. It has been reported by earlier researchers [10,19–21] that graphite transforms to an amorphous form during high energy mechanical milling (e.g. within ∼2 h of milling in SPEX 8000 shaker mill). The present results clearly suggest that the resin solution, which is expected to be absorbed and coated on the newly formed surfaces of the particles generated by the processes of repeated cold welding and fracture during mechanical milling, acts as a diffusion barrier to the interfacial diffusion reaction between graphite and Si to form electrochemically inactive SiC. Furthermore, it also reduces the amorphization kinetics of graphite.

The SEM secondary electron image of 15 h milled sample, shown in Fig. 2a, indicates the formation of irregularly shaped fine particles (<0.5 μm) which are expected to be coated by the resin due to the good wettability of the resin solution with the Si and graphite particles, and the outstanding adhesive properties of the epoxy resin. The elemental composition determined by microanalysis using energy dispersive X-ray spectroscopy, shown in Fig. 2b, indicates the presence of carbon, silicon and iron in the 15 h milled sample. Quantitative analysis of the elemental composition obtained by EDS is presented in Table 1. Appearance of the Fe peak in the EDS (Fig. 2b) mainly arises from the iron contamination in the 15 h milled sample due to the SS milling media caused by frictional wear due to impingement of the harder Si and graphite particles with the relatively soft SS balls and the SS walls of the container.

Iron contamination from the milling media in the as-milled sample could not be observed in the XRD patterns (Fig. 1) mainly due to the highly nanocrystalline nature of iron and convolution of the most intense bcc iron peak ($2\theta = 44.6^\circ$) with the graphite peak. In order to determine the distribution of the C and Si, elemental X-ray mapping has been used and the result is shown in Fig. 2c and d. The elemental X-ray maps of C and Si combined with the SE image (Fig. 2a) show that the electrochemically active Si particles are homogeneously dispersed and distributed on the graphite matrix. During high energy mechanical milling of graphite and silicon, it can be expected that the harder silicon particles gets fragmented and embedded in the

Table 1
Elemental composition and specific surface area of C–18 wt.% Si–40 wt.% resin generated after 15 h of milling and after thermal treatment at 773 K, 973 K, 1073 K and 1173 K for 6 h each in UHP-Ar

	C (wt.%)	Si (wt.%)	Fe (wt.%)	Specific surface area ($m^2\ g^{-1}$)
15 h	78.39	17.44	4.17	18
773 K	74.20	20.76	5.04	105
973 K	70.00	24.43	5.57	125
1073 K	69.20	25.13	5.67	110
1173 K	70.12	24.29	5.59	106

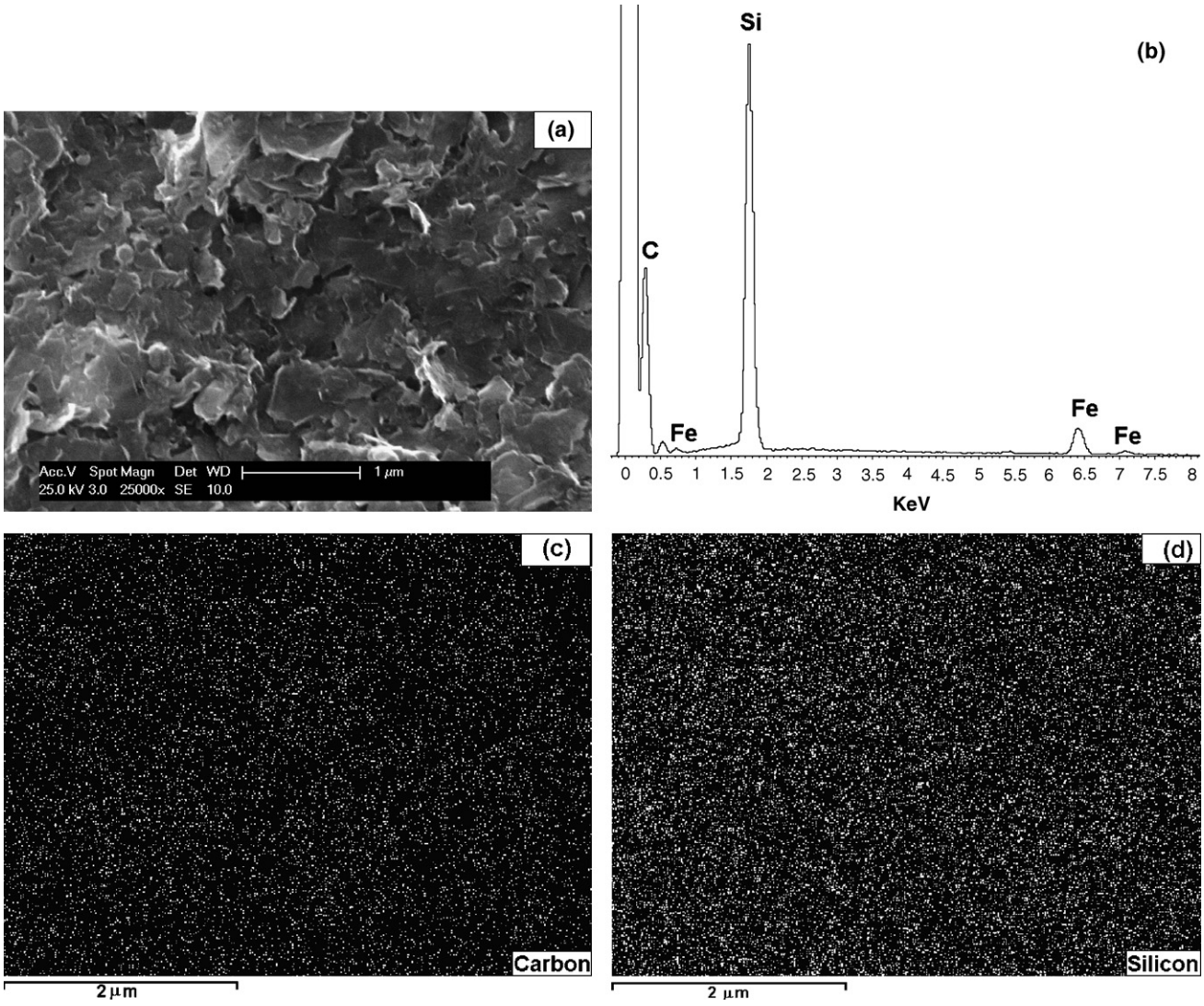

Fig. 2. SEM secondary electron image (a), EDS spectra (b), and X-ray elemental map of C (c) and Si (d) of C–18 wt.% Si–40 wt.% resin obtained after 15 h of milling.

softer graphite matrix. The TEM bright field image, shown in Fig. 3, confirms that the nanocrystalline Si (∼10 nm) is embedded and homogenously distributed on the softer graphite matrix resulting in an intra-type nanocomposite.

The results above show that the resin prevents the formation of electrochemically inactive SiC, and also reduces the amorphization kinetics of graphite during prolonged milling of Si and graphite. However, the presence of resin is undesirable in the final product due to its poor electrical conductivity and poor lithium ion diffusivity which is expected to deteriorate the electrode performance of the nanocomposite. Hence, it is necessary to pyrolyze and convert the resin to an electrically conductive and lithium ion diffusive amorphous carbon by thermal decomposition [22,23] at a suitable temperature to prevent the formation of SiC. In order to identify the decomposition temperature and weight loss of the resin, DTA/TGA has been performed for pure poly[(*o*-cresyl glycidyl ether)-*co*-formaldehyde] resin. The DTA curve of pure resin, shown in Fig. 4, shows a sharp exothermic peak at around 648 K. On the other hand, the TGA result (Fig. 4) shows a significant weight loss (∼72%) in the temperature region 550–800 K which corresponds to the carbonization step of the resin to form amorphous hard carbon [24,25]. The carbonization level continues to increase with increasing temperatures due to a series of complex chemical reactions such as, condensation, dehydrogenation, aromatization, re-organization, decomposition, etc. [24,25]. The TGA curve also shows a ∼22% weight loss in the temperature range of 800–1173 K which mainly arises due to the removal of the residual hydrogen/oxygen species from the resin derived amorphous carbon [22–25]. These results are in agreement with reports indicating [22–25] that an amorphous carbon skeleton with minimal amount of hydrogen/oxygen is formed after thermal treatment at and above ∼973 K. The thermal analysis results thus were also be used to ascertain the composition of the nanocomposite after thermal treatment.

Based on the DTA/TGA results, the 15 h milled powder has been thermally treated at 773 K, 973 K, 1073 K and 1173 K for 6 h each in UHP-Ar atmosphere to decompose the resin to form resin based amorphous hard carbon. It has been identified that SiC begins to form when the milled powder is thermally treated

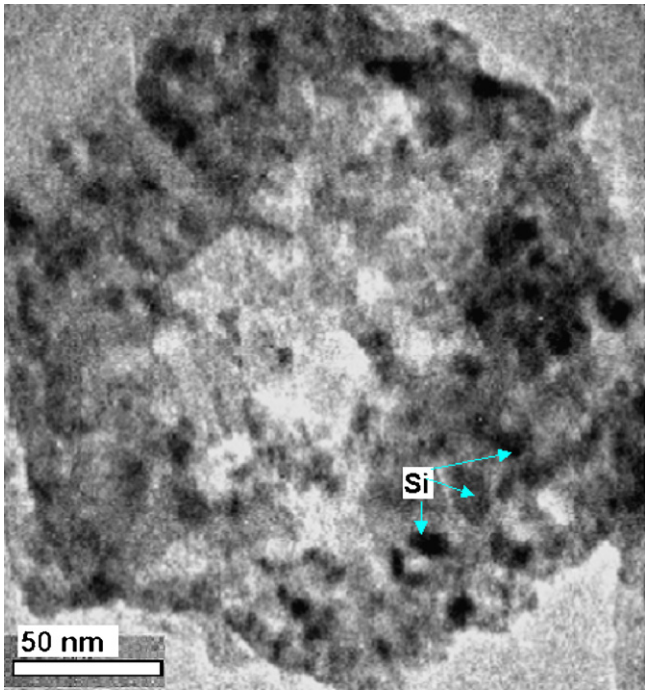

Fig. 3. TEM bright field image shows that the nanoparticle Si is embedded and homogeneously distributed on the graphite matrix of C–18 wt.% Si–40 wt.% resin generated after 15 h of milling.

above 1173 K, and hence thermal treatment has been limited to temperature of 1173 K in the present study. The XRD patterns of the powder thermally treated up to 1173 K, shown in Fig. 1, show the characteristic peaks corresponding to graphite and Si without exhibiting any detectable amount of SiC. However, in addition to Si and graphite, new XRD peaks have been detected in the XRD patterns (Fig. 1) after thermal treatment at and above 773 K. The new XRD peaks observed after thermal treatment at 773 K, 973 K and 1073 K were successfully indexed as bcc iron of lattice parameter ~0.2866 nm. The appearance of the Fe peak in the XRD patterns confirm the EDS result (Fig. 2b) of the 15 h milled sample which shows the presence of nanocrystalline Fe, arising as a contaminant from the stainless steel milling media

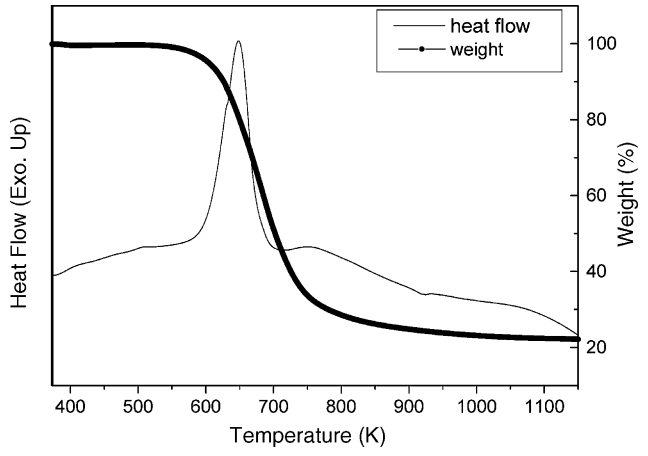

Fig. 4. DTA/TGA traces of poly[(*o*-cresyl glycidyl ether)-*co*-formaldehyde] resin conducted in UHP argon.

due to frictional wear arising from the impingement of the hard Si particles with the SS balls and the SS walls of the container. The nanocrystalline iron is supposed to undergo significant grain growth at temperatures only above ~700 K [26,27] and therefore the XRD peaks of iron has been detected in the present experiment after thermal treatment of the milled powder at and above 773 K. At the same time, the new XRD peaks observed at 1173 K has been indexed as ordered B2 Fe_3Si which suggest that the iron contaminant reacts with silicon at high temperatures to form iron silicides, consequently reducing the amount of active silicon in the nanocomposite. The thermally treated powder of nominal composition C–18 wt.% Si–40 wt.% resin thereafter will be denoted as Si/C/HC nanocomposite. The composition of the Si/C/HC nanocomposite obtained after thermal treatment at 1173 K is estimated based on the 23% yield of amorphous HC obtained from the resin determined by thermal analysis (Fig. 4), considering no weight loss of Si and graphite during the thermal treatment. The composition of the nanocomposite is determined to be approximately C–26 wt.% Si–13.3 wt.% HC. However, taking into consideration the 5.6 wt.% Fe contamination from the milling media, analyzed by EDS after thermal treatment at 1173 K (Table 1), the composition of the Si/C/HC composite synthesized after thermal treatment at 1173 K can be estimated to be approximately C–24.5 wt.% Si–12.5 wt.% HC–5.6 wt.% Fe.

In order to study the change in the size, shape and microstructure of the particles after thermal treatment at various temperatures, SEM investigation has been conducted on the Si/C/HC nanocomposite obtained after thermal treatment at different temperatures. Fig. 5 shows the SEM secondary electron image of Si/C/HC nanocomposite synthesized after thermal treatment for 6 h each at 773 K, 973 K, 1073 K and 1173 K in UHP-Ar, respectively. The secondary electron images (Figs. 2a and 5) show that there is no significant change in the particle size, shape and morphology of Si/C/HC composite with increase in temperature up to 973 K. However, a minimal particle growth has been observed with increase in temperature above 973 K which may be due to the interparticle interaction due to the expected physical and chemical affinity between the graphite matrix and the amorphous hard carbon. The specific surface area of the Si/C/HC composite synthesized at various temperatures along with the 15 h milled powder, measured by BET, is tabulated in Table 1. The specific surface area of the Si/C/HC nanocomposite synthesized after thermal treatment at 773 K increases significantly (~105 $m^2\ g^{-1}$) in comparison to the mechanically milled powder (~18 $m^2\ g^{-1}$) due to the decomposition of the resin to form a highly porous amorphous hard carbon [24,25]. With further increase in the annealing temperature to 973 K, the specific surface area subsequently increases to ~125 $m^2\ g^{-1}$ which may be due to the higher amorphous carbon yield from the resin with increase in temperature. A minimal reduction in specific surface area (~110 $m^2\ g^{-1}$ at 1073 K and ~106 $m^2\ g^{-1}$ at 1173 K) with further increase in temperature above 973 K may be a result of the minimal particle growth above 973 K.

The elemental composition analysis obtained by EDS of Si/C/HC composite obtained after thermal treatment at 773 K, 973 K, 1073 K and 1173 K (shown in Fig. 6 as an example for

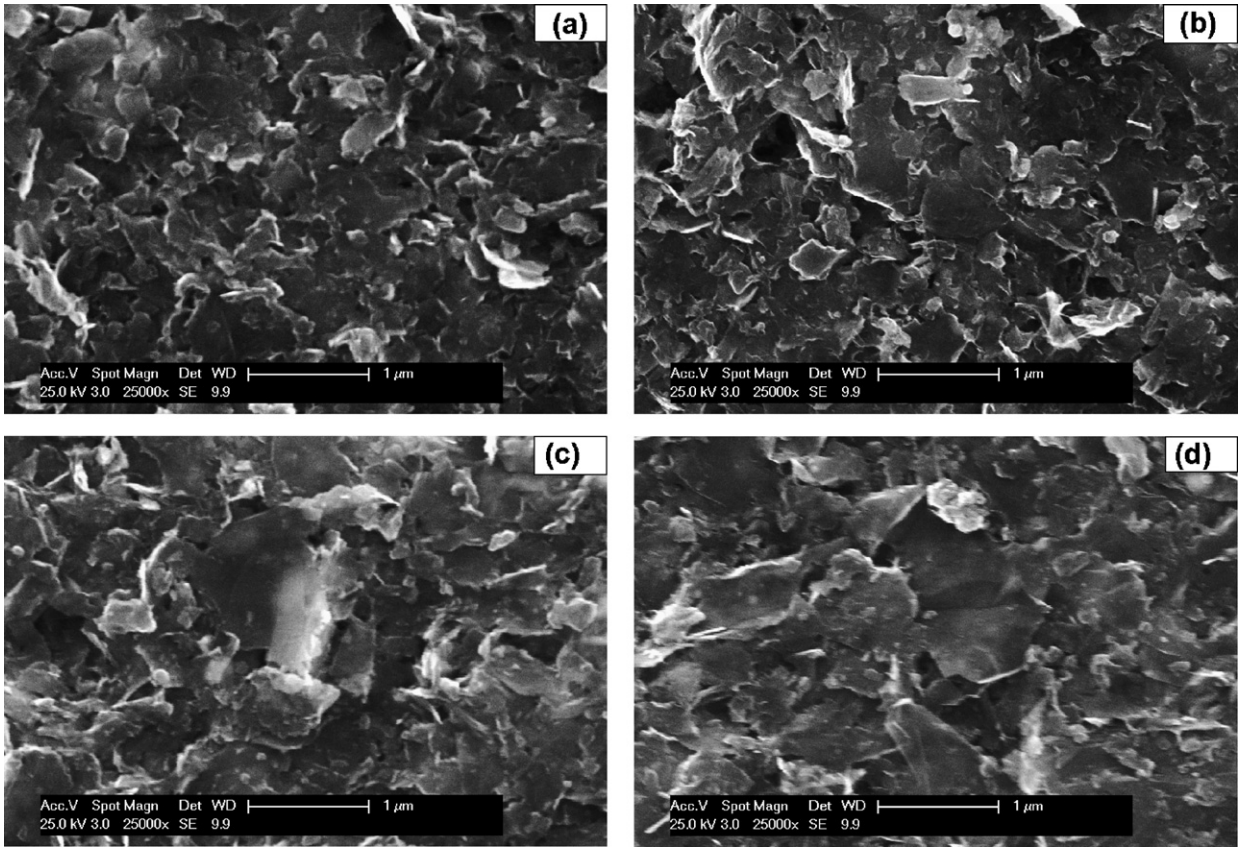

Fig. 5. SEM secondary electron images of C–18 wt.% Si–40 wt.% resin generated after 15 h of milling and after thermal treatment at 773 K (a), 973 K (b), 1073 K (c) and 1173 K (d) for 6 h each in UHP argon.

composite heat treated at 1173 K for 6 h) indicates the presence of carbon, silicon and iron, and the quantitative estimate of the elemental composition is tabulated in Table 1. The elemental composition of the Si/C/HC composite obtained after thermal treatment at 973 K, 1073 K and 1173 K is in good agreement with the estimated composition that has been calculated from the starting composition and the yield of amorphous hard carbon derived from resin obtained by thermal analysis measurement discussed earlier for the sample treated at 1173 K. This result clearly suggests that the carbonization of the resin is nearly complete after thermal treatment at 973 K, 1073 K and 1173 K. The elemental X-ray maps of C and Si of Si/C/HC nanocomposite synthesized after thermal treatment at 773 K, 973 K, 1073 K and 1173 K, which are similar to the X-ray maps of C and Si of mechanically milled sample (Fig. 2c and d), indicates that the Si particles are homogeneously dispersed and distributed within the graphite matrix after thermal treatments. The TEM bright field image (Fig. 7) of Si/C/HC composite synthesized at 1173 K confirms that the nanocrystalline Si (∼25 nm) is embedded and homogeneously distributed within the graphite matrix. This result clearly indicates that the increase in particle size with increasing temperature is only marginal for nanocrystalline silicon (from ∼10 nm in the as-milled state to ∼25 nm at 1173 K) in the Si/C/HC nanocomposite. The presence of graphitic carbon and amorphous hard carbon in Si/C/HC composite can therefore be expected to serve as grain growth inhibitors preventing interparticle growth causing coarsening of Si nanoparticle in the resulting Si/C/HC nanocomposite.

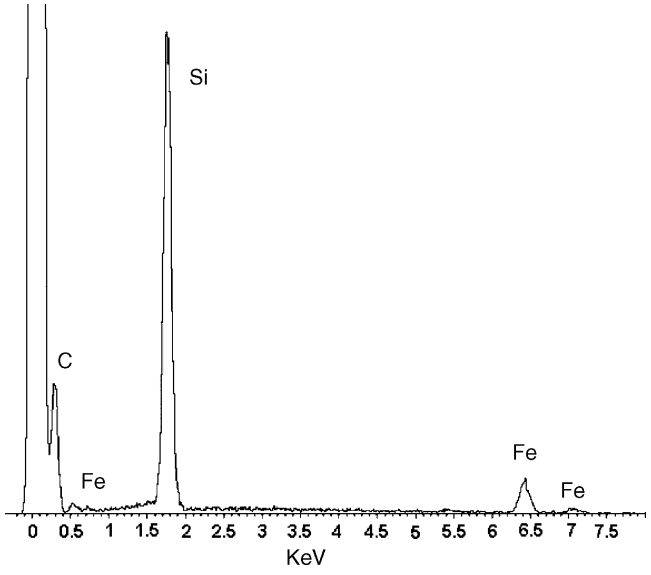

Fig. 6. The EDS spectra of Si/C/HC composite taken on the SEM image in Fig. 5d for the composite obtained after thermal treatment at 1173 K in UHP-Ar for 6 h.

Electrochemical studies have been conducted for the Si/C/HC nanocomposite to explore its potential as a lithium ion anode. The nanocomposites synthesized after thermal treatment at 973 K, 1073 K and 1173 K each for 6 h in UHP-Ar were tested for

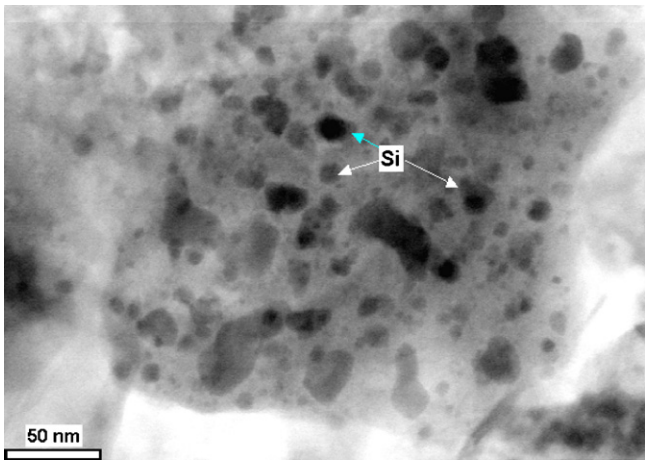

Fig. 7. TEM bright field image shows that the nanoparticle Si is embedded and homogeneously distributed on the graphite matrix of C/Si/HC nanocomposite synthesized after thermal treatment at 1173 K in UHP-Ar for 6 h.

their electrochemical characteristics since the decomposition of the resin is expected to nearly complete at the above-mentioned temperatures. Fig. 8 shows the variation of specific capacity versus cycle number of the Si/C/HC nanocomposites synthesized at 973 K, 1073 K and 1173 K, respectively, cycled at a constant current of 160 mA g^{-1}. As shown in Fig. 8, the first discharge and first charge capacity of the Si/C/HC nanocomposite decreases with increasing annealing temperature. The first charge capacity of the Si/C/HC nanocomposite obtained after thermal treatment at 973 K (~833 mAh g^{-1}) is ~9% and ~28% higher than the Si/C/HC nanocomposite obtained after thermal treatment at 1073 K (~757 mAh g^{-1}) and 1173 K (~599 mAh g^{-1}), respectively. This result clearly suggests that the weight fraction of the active Si phase decreases significantly after thermal treatment at 1173 K due to the reaction of silicon with the iron contaminant to form the inactive iron silicides B2 Fe_3Si during thermal treatment at 1173 K which is in good agreement with the XRD results (Fig. 1). On the other hand, the irreversible loss in the first cycle for the Si/C/HC nanocomposite, plotted in Fig. 9, decreases with

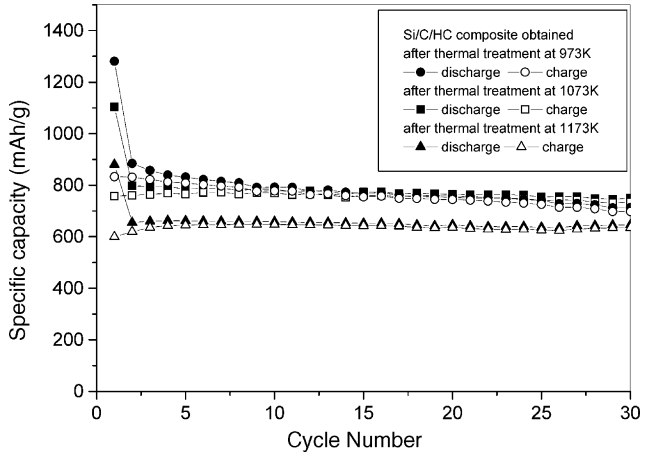

Fig. 8. Specific capacity vs. cycle numbers of the Si/C/HC derived nanocomposite electrode obtained after thermal treatment at 973, 1073 and 1173 K in UHP-Ar for 6 h each, and cycled at a constant current of 160 mA g^{-1}.

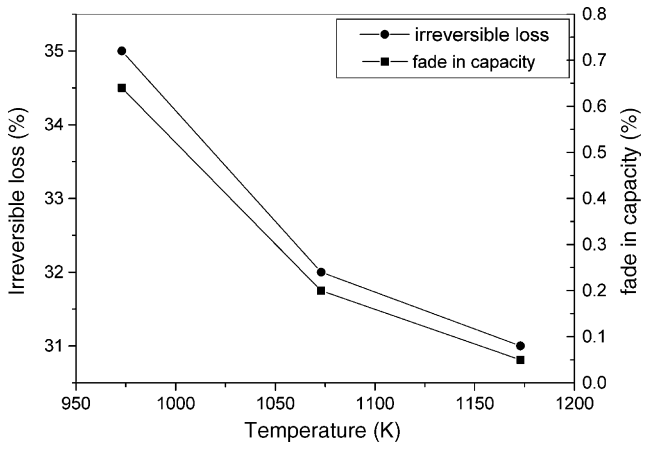

Fig. 9. Variation in fade in capacity (%) and irreversible loss of Si/C/HC nanocomposite obtained after thermal treatment at different temperatures.

increasing heat treatment temperature. This can be expected due to the reduced extent of the solid–electrolyte interface reaction occurring due to a decrease in the specific surface area with increase in temperature (Table 1). The decreasing amount of hydrogen/oxygen species, which react with Li irreversibly [22,23], with increasing annealing temperature probably also contributes to the reduction in the irreversible loss with increasing heat treatment temperatures.

The percentage fade in capacity per cycle of the Si/C/HC nanocomposites as a function of heat treatment temperature has also been plotted in Fig. 9. The retention in capacity significantly improves with increasing heat treatment temperature. For example, the Si/C/HC nanocomposite obtained after heat treatment at 973 K and 1073 K shows a fade in capacity of 0.64% and 0.2% loss per cycle, respectively, whereas the Si/C/HC nanocomposite obtained after thermal treatment at 1173 K exhibits a loss in capacity of only 0.05% loss per cycle. Based on the above electrochemical results, it can be concluded that the Si/C/HC nanocomposite synthesized after thermal treatment at 1173 K is promising as an anode for lithium ion applications due to the low fade in capacity as well as low irreversible loss in comparison to the Si/C/HC nanocomposite obtained after thermal treatment at 973 K and 1073 K. The Si/C/HC nanocomposite obtained after thermal treatment at 1173 K shows a first discharge and first charge capacity ~880 and ~599 mAh g^{-1}, respectively, with an irreversible loss of ~31%. As shown in Fig. 8, the reversible capacity increases with subsequent cycles and after the fourth cycle the nanocomposite exhibits an optimal reversible capacity ~640 mAh g^{-1} with excellent capacity retention up to 30 cycles.

In order to study the rate capability of the Si/C/HC nanocomposite synthesized at 1173 K, the nanocomposite has been discharged/charged at different rates of 40 mAh g^{-1}, 80 mAh g^{-1} and 120 mAh g^{-1} in addition to 160 mAh g^{-1}. The variation in specific capacity versus cycle number of the Si/C/HC nanocomposite cycled at different rates is shown in Fig. 10. The variation of first discharge, first charge and second discharge of the Si/C/HC nanocomposite synthesized at 1173 K, plotted in Fig. 11, decreases almost linearly with increasing discharge/charge rate. For example, the first charge capacity decreases with increasing discharge/charge rate and the vari-

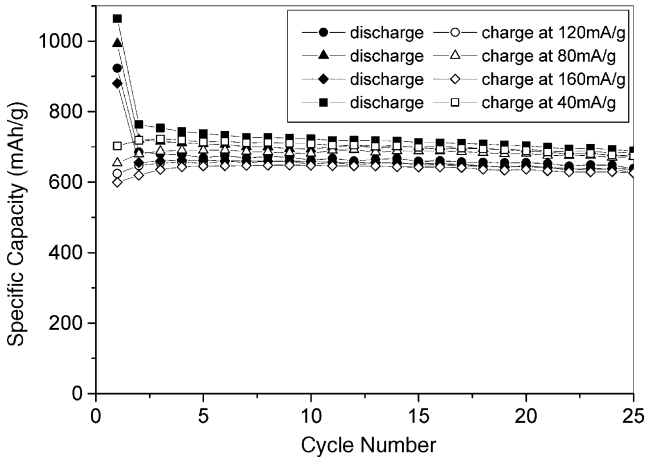

Fig. 10. Specific capacity vs. cycle numbers of Si/C/HC derived nanocomposite electrode obtained after thermal treatment in UHP-Ar for 6 h at 1173 K at a different rate of 40, 80, 120 and 160 mA g^{-1}.

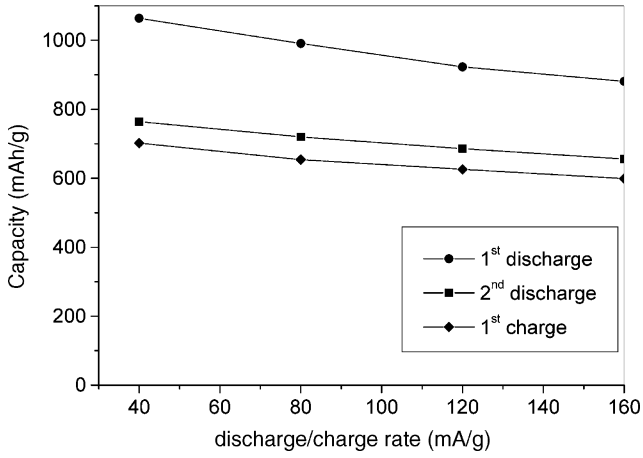

Fig. 11. Variation of the first discharge, first charge and second discharge capacity of Si/C/HC nanocomposite cycled at different rates.

ation in capacity can be related to a rate equation given by $Y = 729\ \text{mAh g}^{-1} - 0.8425X\ \text{mAh g}^{-1}$, where Y and X denote the first charge capacity (mAh g^{-1}) and the discharge/charge rate (mA g^{-1}), respectively. From the above equation, the expected first charge capacity of the Si/C/HC nanocomposite at very slow discharge/charge rate ($X \sim 0$ mA g^{-1}) can be extrapolated to be ~729 mAh g^{-1}. The capacity retained at the discharge/charge rate of 160 mA g^{-1} is ~599 mAg g^{-1} which is about 82% of that capacity (~729 mAh g^{-1}) thus indicating that the Si/C/HC is a promising anode material for lithium battery application for moderately high charge/discharge rates. The decrease in specific capacity with increasing charge/discharge rate mainly arises due to the slow rate of diffusion of Li through the composite. The diffusion rate and as a result, the rate capability is expected to be enhanced with reduction in the particle size at the nanometer level where diffusion will be dictated mainly by grain boundary diffusion rather than bulk diffusion [28,29]. In addition, the use of SFG synthetic graphite [30] instead of natural graphite as a matrix could improve the rate capability of the Si/C/HC composite due to its demonstrated high rate capability.

The differential capacity plot of the Si/C/HC nanocomposite obtained after thermal treatment at 1173 K (Fig. 12a), cycled at a rate of 160 mA g^{-1}, shows that in addition to silicon, graphite/HC also has significant contribution on the overall capacity of the nanocomposite. The reversible capacities of graphite and resin based hard carbon determined from individual testing of cells were ~300 mAh g^{-1} (at ~C/10 rate) and ~250 mAh g^{-1} (at ~C/10 rate), respectively. Therefore, the expected contribution on the overall capacity of the nanocomposite due to the presence of electrochemically active graphite (~57.4 wt.%) and resin based HC (~12.5 wt.%) in the nanocomposite is approximately ~200 mAh g^{-1}. Hence, the enhanced reversible capacity of Si/C/HC nanocomposite arises mainly from the Si nanoparticle. The appearance of peaks corresponding to ~0.09, ~0.24 and ~0.29 V after the first cycle suggests that the crystalline Si transforms to amorphous Si after the first cycle. After the first cycle, the peak intensity corresponding to the reaction of Li ion with amorphous Si (~0.24 and ~0.29 V) and graphite remains almost unchanged with cycling (Fig. 12b) which suggests the excellent capacity retention of the nanocomposite with cycling. The excellent capacity retention of the Si/C/HC nanocomposite observed is probably due to the

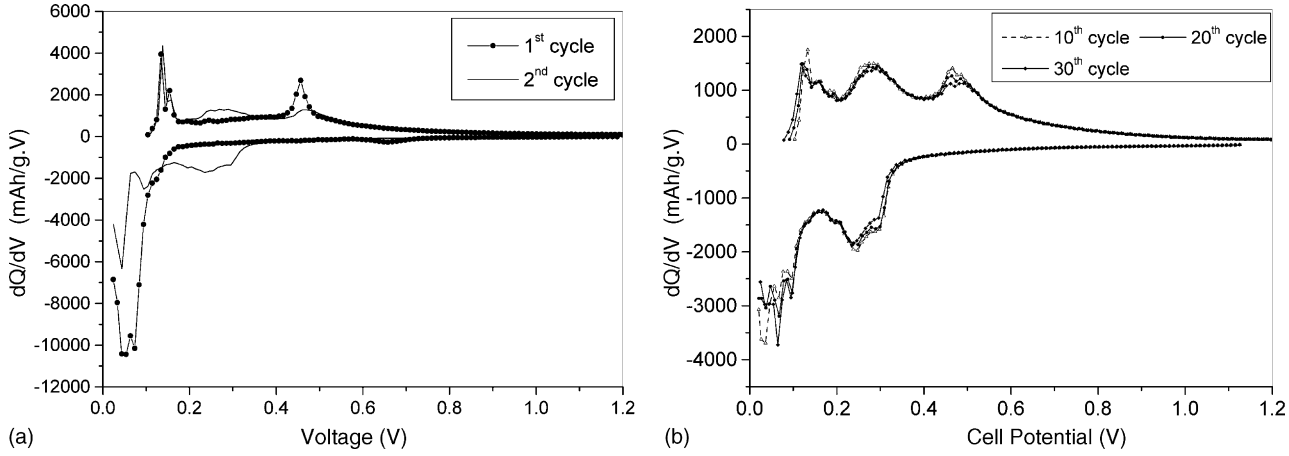

Fig. 12. Differential capacity vs. cell potential curves of the Si/C/HC nanocomposite electrode synthesized by thermal treatment in UHP-Ar for 6 h at 1173 K (a) after 1st and 2nd cycle and (b) after 10th, 20th and 30th cycles.

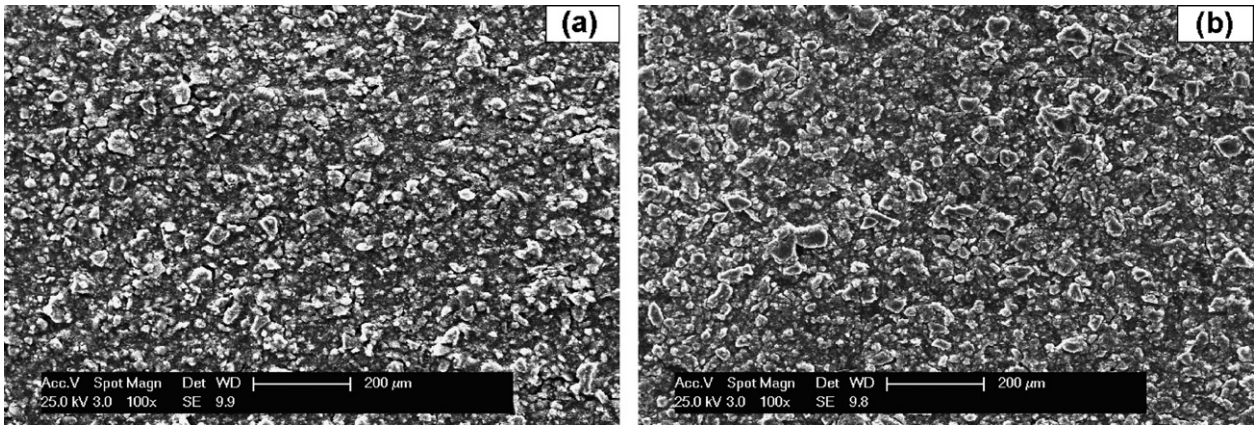

Fig. 13. SEM micrograph of the Si/C/HC electrode obtained after thermal treatment in UHP-Ar for 6 h at 1173 K (a) before and (b) after cycling for 30 cycles.

maintenance of the structural integrity of the electrode during the alloying and dealloying processes.

The SEM secondary electron image of the uncycled and cycled samples of Si/C/HC nanocomposite obtained after thermal treatment at 1173 K, shown in Fig. 13, indicates the excellent structural integrity of the electrode even after 30 cycles. However, in order to study the possible debonding of Si particles from the graphite matrix and/or the failure of the graphite matrix, which can deteriorate the electrode performance during repeated charge/discharge processes, SEM images of the electrode have been obtained at a higher magnification. Fig. 14a and b shows the higher magnification secondary electron SEM image of the Si/C/HC nanocomposite before and after cycling. There appears to be no significant change in microstructure or morphology of the particles although the formation of the thick solid electrolyte interphase (SEI) on the particle surface appears to be evident.

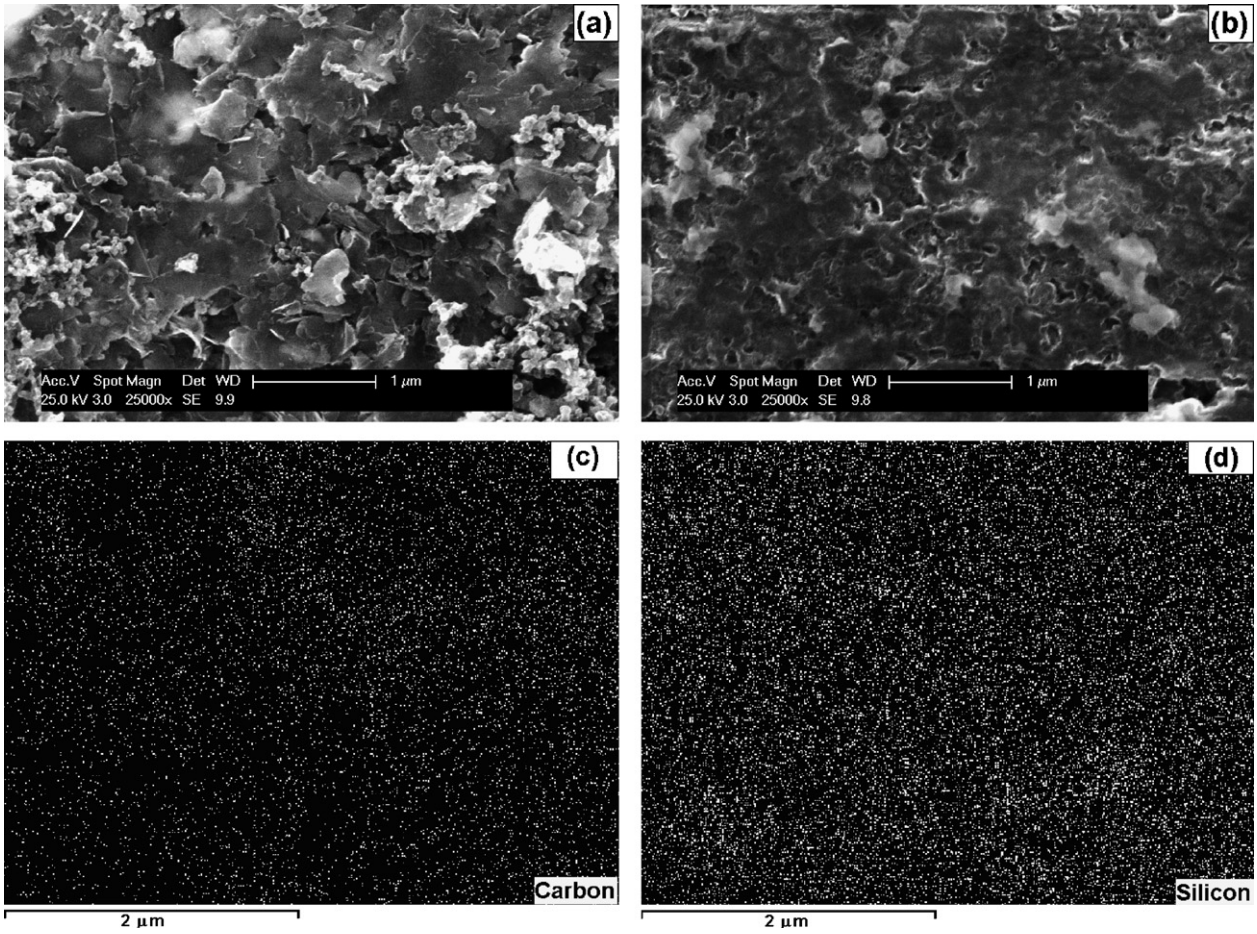

Fig. 14. High magnification SEM micrograph of Si/C/HC electrode, obtained after thermal treatment in UHP-Ar for 6 h at 1173 K, (a) before and (b) after cycling for 30 cycles, and X-ray elemental map of (c) C and (d) Si of Si/C/HC electrode after cycling for 30 cycles.

The SEI film which is conductive to lithium ions but electronically insulating, is formed due to the reductive decomposition of the electrolyte solution on the surface of the particle in the initial state of charging [31,32]. It is also possible that the SEI layer contributes to the excellent capacity retention of this nanocomposite. In order to identify the distribution of graphite and silicon of the underlying Si/C/HC nanocomposite covered by SEI layer, the X-ray mapping of carbon and silicon has been performed on the cycled electrode. The X-ray maps of C and Si obtained from the Si/C/HC nanocomposite obtained after heat treatment at 1173 K cycled for 30 cycles (Fig. 14c and d) show that the Si particle is still homogeneously dispersed and distributed on the graphite matrix without any segregation which suggested that there is no significant debonding of silicon from the graphite matrix during cycling. The X-ray maps of graphite and silicon after cycling also suggests that there is no structural failure of the underlying Si/C/HC composite covered by SEI layer. This result clearly suggests that the structural integrity (no debonding of Si particles or failure of the matrix) of Si/C/HC nanocomposite synthesized after thermal treatment at 1173 K is maintained during the repeated alloying and dealloying processes.

The excellent structural integrity of the Si/C/HC nanocomposite synthesized after thermal treatment at 1173 K is expected to arise due to the homogeneous dispersion and distribution of Si within the graphite matrix during extended milling. In addition, the solution coating by the resin is expected to enhance the wettability between graphite and the embedded Si during mechanical milling, and as a result, the amorphous HC obtained by thermal decomposition of the resin may improve the mechanical properties of the composite by enhancing the interface adhesion/bonding between Si and graphite arising due to the preferred chemical affinity between the graphite matrix and the amorphous hard carbon. With increase in the heat treatment temperature it is expected that the interface strength between graphite and silicon is enhanced due to the stronger interface bonding. Thus, the resin based amorphous hard carbon coating is expected to improve the capacity retention with increase in temperature due to enhancement of the interface strength between graphite and silicon. The amorphous hard carbon coating on each and every individual particle is also expected to improve the fatigue strength of the Si/C/HC nanocomposite due to the generation of a compressive stress on the Si/C core. The compressive stress within the core by amorphous hard carbon coating may result in the enhancement of the cycle life of the composite which typically experiences progressive stress/strain cycles during the repeated alloying/dealloying processes. However, further studies are necessary to understand the influence of these structural aspects on the mechanical property of the nanocomposite. More studies are also warranted to determine the exact role of the resin derived amorphous HC in enhancing the cycling stability of the Si/C/HC composites.

4. Conclusion

An intra-type nanocomposite based on graphite as a matrix and silicon nanoparticle as a dispersoid, coated with amorphous hard carbon, has been synthesized as a suitable anode material for lithium ion batteries. High energy mechanical milling has been performed on graphite and silicon particles in the presence of the poly[(*o*-cresyl glycidyl ether)-*co*-formaldehyde] epoxy resin to form the graphite, silicon and amorphous hard carbon based nanocomposite. The epoxy resin acts as a diffusion barrier to the interfacial reaction between graphite and silicon to form the electrochemically inactive SiC. Each individual particle is expected to be coated with epoxy resin due to its good wettability and excellent adhesive properties with metallic particles. The SEM, EDS, X-ray mapping and TEM investigation has confirmed that the nanoparticle silicon (∼10 nm) formed by the repeated process of fracture during mechanical milling, is embedded and homogeneously dispersed on the graphite matrix. In order to decompose the epoxy resin to electrically conductive and lithium ion diffusive amorphous hard carbon, the mechanically milled powder is thermally treated at 973 K, 1073 K and 1173 K for 6 h in ultrahigh purity argon atmosphere, respectively. Therefore, an intra-type nanocomposite based on graphite and silicon coated with resin based amorphous hard carbon, denoted as Si/C/HC, is obtained after thermal treatment of mechanically milled powder at 973 K, 1073 K and 1173 K for 6 h. The interface strength/adhesion between graphite and embedded silicon, coated with amorphous hard carbon, is expected to increase with increase in temperature due to enhancement of the interface bonding with increase in temperature. The electrochemical studies have revealed that the Si/C/HC nanocomposite synthesized after thermal treatment at 1173 K for 6 h exhibit low fade in capacity (∼0.05% loss per cycle) and low irreversible loss (∼31%) in comparison to the Si/C/HC nanocomposite obtained after thermal treatment at 973 K and 1073 K. The resultant Si/C/HC based nanocomposite anodes obtained after thermal treatment at 1173 K exhibit a stable capacity of ∼640 mAh g^{-1} with an excellent capacity retention (∼0.05% loss per cycle) when cycled at a rate of ∼160 mA g^{-1}. The nanocomposite anode obtained at 1173 K also shows a moderate rate capability when cycled at different discharge/charge rates (∼40–160 mA g^{-1}). Scanning electron microscopy and X-ray mapping analyses indicate that the structural integrity and the microstructural stability of the nanocomposite during the alloying/dealloying process appear to be the main reasons contributing to the good cyclability observed in the Si/C/HC nanocomposites synthesized after thermal treatment at 1173 K.

Acknowledgements

The authors would like to thank NSF (Grants CTS-9700343 and CTS-0000563) and NASA (NAG3-2640) for financial support of this research.

References

[1] Z. Ogumi, M. Inaba, in: W.A. Schalkwijk, B. Scrosati (Eds.), “Carbon Anodes” in Advances in Lithium Ion Batteries, Kluwer Academic, New York, 2002, pp. 79–101.
[2] J.L. Tirado, Mater. Sci. Eng. R 40 (2003) 103.
[3] J. Maranchi, O.I. Velikokhatnyi, M.K. Datta, I.S. Kim, P.N. Kumta, in: B. Lee, S. Komarneni (Eds.), Chemical Processing of Ceramics, second ed., CRC Press, Taylor and Francis, 2005, p. 667.

[4] M. Winter, J.O. Besenhard, Electrochim. Acta 45 (1999) 31.
[5] L.Y. Beaulieu, K.W. Eberman, R.L. Turner, L.J. Krause, J.R. Dahn, Electrochem. Solid-State Lett. 4 (2001) A137.
[6] O. Mao, R.L. Turner, I.A. Courtney, B.D. Fredericksen, M.I. Buckett, L.J. Krause, J.R. Dahn, Electrochem. Solid-State Lett. 2 (1999) 3.
[7] I.-S. Kim, G.E. Blomgren, P.N. Kumta, J. Power Sources 130 (2004) 275.
[8] I.-S. Kim, P.N. Kumta, G.E. Blomgren, Electrochem. Solid-State Lett. 3 (2000) 493.
[9] I.-S. Kim, G.E. Blomgren, P.N. Kumta, Electrochem. Solid-State Lett. 6 (2003) A157.
[10] M.K. Datta, P.N. Kumta, J. Power Sources 158 (2006) 557.
[11] J. Yang, B.F. Wang, K. Wang, Y. Liu, J.Y. Xie, Z.S. Wen, Electrochem. Solid-State Lett. 6 (2003) A154.
[12] I.-S. Kim, P.N. Kumta, J. Power Sources 136 (2004) 145.
[13] H. Uon, B.C. Kim, T. Fuse, M. Ue, J. Yamaki, J. Electrochem. Soc. 153 (2006) A1708.
[14] H. Li, X. Huang, L. Chen, Z. Wu, Y. Liang, Electrochem. Solid-State Lett. 2 (1999) 547.
[15] G.X. Wang, J. Yao, H.K. Liu, Electrochem. Solid-State Lett. 7 (2004) A250.
[16] K.J. Gross, J.C.F. Wang, G.A. Roberts, US Pat. Appl. Pub. US2004/137327 A1 (2004).
[17] C.S. Wang, G.T. Wu, X.B. Zhang, Z.F. Qi, W.Z. Li, J. Electrochem. Soc. 145 (1998) 2751.
[18] M. Sherif El-Eskandarany, K. Sumiyama, K. Suzuki, J. Mater. Res. 10 (1995) 659.
[19] X.Y. Yang, Z.W. Huang, Y.K. Wu, H.Q. Ye, Mater. Sci. Eng. A 300 (2001) 278.
[20] J. Tang, W. Zhao, L. Li, A.U. Falster, W.B. Simmons, W.L. Zhou, Y. Ikuhara, J.H. Zhang, J. Mater. Res. 11 (1996) 733.
[21] J.Y. Huang, Acta Mater. 47 (1999) 1801.
[22] Y. Liu, J.S. Xue, T. Zheng, J.R. Dahn, Carbon 34 (1996) 193.
[23] J.R. Dahn, T. Zheng, Y. Liu, J.S. Xue, Science 270 (1995) 590.
[24] K.A. Trick, T.E. Saliba, Carbon 33 (1995) 1509.
[25] C.N. Cascaval, Eur. Polym. J. 30 (1994) 969.
[26] E. Bonetti, L. del Bianco, L. Pasquini, E. Sampaolesi, Nanostruct. Mater. 12 (1999) 685.
[27] T.R. Malow, C.C. Koch, Acta Mater. 45 (1997) 2177.
[28] I.V. Belova, G.E. Murch, J. Metastable Nanocrystall. Mater. 19 (2004) 25.
[29] I.A. Ovidko, A.G. Sheinerman, Philos. Mag. 83 (2003) 1551.
[30] H. Buqa, D. Goers, M. Holzapfel, M.E. Spahr, P. Novak, J. Electro. Soc. 152 (2005) A474.
[31] D. Aurbach, in: W.A. Schalkwijk, B. Scrosati (Eds.), Advances in Lithium Ion Batteries, Kluwer Academic, New York, 2002, pp. 79–101.
[32] P.B. Balbuena, Y. Wang (Eds.), Lithium Ion Batteries–Solid Electrolyte Interphase, Imperial College Press, London, 2004.